Deformation and damage due to drying-induced salt crystallization in porous limestone

Hannelore Derluyn[a,b,*], Peter Moonen[a,b], Jan Carmeliet[a,b]

[a] *ETH Zurich, Chair of Building Physics, Wolfgang-Pauli-Strasse 15, 8093 Zürich, Switzerland*
[b] *EMPA, Swiss Federal Laboratories for Materials Science and Technology, Laboratory for Building Science and Technology, Überlandstrasse 129, 8600 Dübendorf, Switzerland*

Abstract

This paper presents a computational model coupling heat, water and salt ion transport, salt crystallization, deformation and damage in porous materials. We focus on crystallization-induced damage. The theory of poromechanics is employed to relate stress, induced by crystallization processes or hygro-thermal origin, to the material's mechanical response. A non-local formulation is developed to describe the crystallization kinetics. The model performance is illustrated by simulating the damage caused by sodium chloride crystallization in a porous limestone. The results are compared with experimental observations based on neutron and X-ray imaging. The simulation results suggest that the crystallization kinetics in porous materials have to be accurately understood in order to be able to control salt dam-

*Corresponding author: tel: +41 58 765 4722; email: hderluyn@gmail.com;
address until 30 Sep.'13: EMPA Dübendorf, Überlandstrasse 129, 8600 Dübendorf, Switzerland
address from 1 Oct.'13: Ghent University, Department of Geology and Soil Science - UGCT, Krijgslaan 281, S8, 9000 Gent, Belgium
Email addresses: hderluyn@gmail.com (Hannelore Derluyn), moonen@arch.ethz.ch, peter.moonen@empa.ch (Peter Moonen), carmeliet@arch.ethz.ch, jan.carmeliet@empa.ch (Jan Carmeliet)

age. The results show that the effective stress caused by salt crystallization depends not only on the crystallization pressure but also on the amount of salt crystals, which is determined by the spreading of crystals in the porous material and the crystallization kinetics.
Keywords: salt crystallization, A. fracture, B. porous material, C. finite elements, C. nondestructive evaluation

---

1. Introduction

Water and dissolved salt ions may penetrate into building materials due to diffusive and advective transport. Upon changes in the environmental conditions, salt can crystallize at the surface (efflorescence) or inside the material (subflorescence). Subflorescence is accompanied with the development of crystallization pressures, which may lead to spalling and cracking of the material, and thus to a reduction of the lifetime of a construction or monument. Until now, the mechanism of crystallization in confined conditions and the related damage processes, as well as the computational modeling, are still subject of scientific analysis. The availability of a model providing a full coupling between heat-water-salt ion transport, salt crystallization, deformations and damage would however be an important asset for engineers and conservators. It would allow them to assess and compare different maintenance, repair or conservation techniques or to assess the durability of a new building material under different climatic conditions, without having to perform long-term experiments.

Coupled numerical models for heat-water-salt transport and salt crystallization in building materials have been developed and described in the

literature (Espinosa et al., 2007; Nicolai et al., 2007; Koniorczyk, 2012). Theories defining the crystallization pressure that is exerted when salt crystals grow in confined conditions are described as well (Scherer, 1999; Flatt, 2002; Steiger, 2005a,b; Coussy, 2006). Moonen et al. (2010, 2011) developed a model that covers the effect of thermal and hygric changes on the damage behavior of porous media. There remains however a need for bringing together the available approaches within a single unifying framework. It is especially challenging to formulate the coupling between salt crystallization and the mechanical response of the building material and to accurately model the crystallization kinetics in a physically and numerically sound way.

In the next section, we present a fully coupled model for heat, water and salt ion transport, salt crystallization, material deformation and damage in porous media. We briefly recall the modeling of heat and moisture transport (Derluyn, 2012). The modeling of the salt crystallization process, the coupling with the mechanical behavior and the damage criterion are discussed in more detail. In section 3, we summarize experimental observations of damage caused by sodium chloride crystallization, induced by drying of an initially wet limestone (Derluyn, 2012). The material and salt properties, needed as input for the model, are also given. Section 4 comprises the simulation of the performed experiment. Comparison with the experimental data suggests that the crystallization kinetics play an important role in the accurate prediction of salt damage.

2. A coupled model for transport, crystallization, deformation and damage

2.1. Conservation of mass

We consider the porous medium consisting of a superposition of four phases: (1) the solid material matrix, (2) the gas phase, (3) the liquid phase and (4) the crystal phase. In these phases several components can be present. For the gas phase we consider dry air and water vapor, for the liquid phase water and dissolved salt ions. Exchange of water can occur between the liquid and the gas phase due to evaporation or condensation, or between the liquid and the crystal phase when hydrated salt crystals form or dissolve. Exchange of salt ions occurs between the liquid and the crystal phase when crystals precipitate or dissolve. We assume that the dissolved salt does not separate macroscopically in the absence of an electric field. Thus the cations and anions are always transported jointly.

We further assume that the solid phase does not exchange mass with other phases. We consider the gas pressure, p_g, to be constant and equal to the atmospheric pressure. In addition, we consider changes in the water vapor mass to be negligible with respect to changes in the liquid water mass and we assume that salt crystals do not move in the pore space.

Under these assumptions, the mass balance is expressed by:

$$\Phi \frac{\partial \left(S_l \rho_l + S_{cr} \rho_{cr} \right)}{\partial t} = \nabla \cdot \left(\mathbf{K}_l \nabla p_c + \boldsymbol{\delta}_v \nabla p_v \right) \tag{1}$$

with Φ the total accessible porosity, S_l and S_{cr} the liquid and the crystal saturation degree, and ρ_l and ρ_{cr} the density of the liquid phase and of the salt crystal. $\mathbf{K}_l$ is the liquid permeability as function of capillary pressure p_c.

The capillary pressure expresses the pressure difference across the liquid-gas interface and is defined as:

$$p_c = p_l - p_g \tag{2}$$

with p_l the liquid pressure and p_g the (constant) gas pressure. $\boldsymbol{\delta}_v$ is the vapor permeability in function of vapor pressure p_v. The vapor pressure can be expressed in terms of the capillary pressure p_c, the absolute temperature T and the water activity a_w by the modified Kelvin relation:

$$p_v = a_w p_{v,sat} \exp\left(\frac{p_c}{\rho_w R_v T}\right) \tag{3}$$

with $p_{v,sat}$ the saturated vapor pressure, ρ_w the water density and R_v the gas constant for water vapor. The water activity depends on the temperature and the salt concentration and accounts for the change of the vapor pressure in equilibrium with a salt solution, compared to the vapor pressure in equilibrium with pure water. For pure water, the water activity equals 1. The higher the salt concentration gets, the lower the water activity will be, leading to lower vapor pressures.

Under the assumption that the dissolved salt ions are transported together, the mass balance for the salt dissolved in the liquid phase reads:

$$\Phi \frac{\partial \left(S_l \rho_l C\right)}{\partial t} + \Phi \frac{\partial S_{cr} / \bar{V}_{cr}}{\partial t} = \nabla \cdot \left(\rho_l \mathbf{D}_i^l \nabla C\right) + \nabla \cdot \left(C \mathbf{K}_l \nabla p_c\right) \tag{4}$$

with C the salt concentration in mole/kg liquid solution and $\bar{V}_{cr}$ the molar volume of the salt crystal. $\mathbf{D}_i^l$ is the salt diffusion coefficient in the liquid phase.

2.2. Conservation of energy

The global energy balance for the porous medium reads:

$$\frac{\partial \left(\left((1-\Phi) c_{p,s} \rho_s + \Phi c_{p,l} S_l \rho_l + \Phi c_{p,cr} S_{cr} \rho_{cr} \right) (T - T_0) \right)}{\partial t} + \frac{\partial \Phi L_{cr} S_{cr} \rho_{cr}}{\partial t} + \nabla \cdot \mathbf{q}_e = 0 \tag{5}$$

assuming that the enthalpy of water vapor and of dry air are negligible for the application of our model (Janssen, 2002). $c_{p,s}$, $c_{p,l}$ and $c_{p,cr}$ are the specific heat capacities at atmospheric pressure of the solid phase, the liquid phase and the crystal phase, respectively. ρ_s is the density of the solid material matrix, L_{cr} the heat of crystallization and T_0 the reference temperature for the enthalpy, being 0°C (273.15 K).

The heat flux $\mathbf{q}_e$ is a combination of a conductive part and an advective part. The conductive part is given by Fourier's law:

$$\mathbf{q}_{e,c} = -\boldsymbol{\lambda} \nabla T \tag{6}$$

with $\boldsymbol{\lambda}$ the apparent thermal conductivity of the porous material. The advective part is described as:

$$\mathbf{q}_{e,a} = -\left(c_{p,v} \left(T - T_0 \right) + L_v \right) \boldsymbol{\delta}_v \nabla p_v - c_{p,l} \left(T - T_0 \right) \mathbf{K}_l \nabla p_c \tag{7}$$

with $c_{p,v}$ the specific heat capacity of water vapor and L_v the latent heat of evaporation of water.

2.3. Salt crystallization

The salt crystal mass balance reads:

$$\Phi \frac{\partial \left(S_{cr} \rho_{cr} \right)}{\partial t} = e_{crl} \tag{8}$$

where we have to define the mass exchange e_{crl} between the liquid and the crystal phase. This mass exchange is described by the kinetics of salt crystallization or dissolution. It is assumed that the supersaturation U is the driving force for crystallization, and consequently that the mass exchange during crystallization is given by (Espinosa et al., 2008; Koniorczyk, 2010):

$$e_{crl} = \zeta K_{m,cr}(U-1)^{g_{cr}} \quad \text{for} \quad U > U_{thr} \tag{9}$$

where $K_{m,cr}$ and g_{cr} are kinetic parameters and ζ is the fraction of the capillary active pore space filled with salt solution. In order for new crystals to nucleate and grow, the supersaturation has to exceed a threshold value U_{thr}.

Dissolution is described by a similar type of equation, only the kinetic parameters and the threshold value differ:

$$e_{crl} = -\zeta K_{m,diss}(1-U)^{g_{diss}} \quad \text{for} \quad U < 1 \tag{10}$$

For the modeling of the crystallization, besides the kinetics, also the availability of pore volume space needs to be considered. If no space is available for crystals to grow, crystallization will stop and consequently the concentration in the solution will remain higher than when the crystals could grow freely. Moreover, dissolution can only take place as long as there are crystals present. Finally, the presence of crystals at a certain location influences nucleation and growth of crystals at neighboring locations. In order to get a stable numerical method incorporating all these constraints, the mass exchange term e_{crl} is implemented as:

$$\begin{aligned} e_{crl} =& f\left(S_{cr}, 1\right) \cdot \zeta K_{m,cr}(\max\left(U, U_{thr}\right) - U_{thr})^{g_{cr}} + \\ & f\left(S_{cr}, 0\right) \cdot \zeta K_{m,diss}(1 - \min\left(U, 1\right))^{g_{diss}} \end{aligned} \tag{11}$$

where the first term represents crystal growth and the second term represents crystal dissolution.

The function f is introduced to ensure that:

1. Crystallization stops when the available pore volume is occupied by salt crystals: as long as $S_{cr} < 1$, $f(S_{cr}, 1)$ equals 1 and the crystallization kinetics are active. When the pore volume is filled with crystals, $S_{cr} = 1$, no crystallization occurs anymore and consequently $f(S_{cr}, 1)$ equals 0.
2. Dissolution can occur as long as there are still crystals present: as long as $S_{cr} > 0$, $f(S_{cr}, 0)$ equals -1. When all crystals are dissolved and $S_{cr} = 0$, the dissolution kinetics stop and $f(S_{cr}, 0)$ equals 0.

Physically, we would only need a step function to define f. However, as step functions may introduce numerical problems due to their discontinuous nature, we smooth the function f by means of an exponential function:

$$f(x_1, x_2) = \operatorname{sgn}(x_2 - x_1) \cdot \left(1 - \exp\left(-\left|\frac{x_1 - x_2}{HBW}\right|\right)\right) \tag{12}$$

where sgn() represents the signum function, x_1 and x_2 are values, and HBW is a parameter controlling the width over which the step is smeared in the function f. The half-band-width HBW of this function is taken low (HBW=0.01) in order to assure that the exponential function rapidly approaches zero as the difference $|x - r|$ increases and that the function f approximates as close as possible a step function.

The function U_{thr} is defined as:

$$U_{thr} = 1 + (U_{start} - 1) \cdot \exp\left(-\upsilon \bar{S}_{cr}\right) \tag{13}$$

and represents the drop of the crystallization threshold from U_{start} to 1. For

primary crystallization (i.e. if no crystals are present) the supersaturation has to exceed the supersaturation value U_{start} before crystallization starts. The drop from U_{start} to 1 is related to the nucleation and growth kinetics. The nucleation and growth kinetics determine how long a certain supersaturation U is maintained until a sufficient amount of crystals have nucleated and/or sufficiently large crystals have grown so that new crystals start to grow at lower supersaturation levels. These phenomena are incorporated in the parameter υ and the function $\bar{S}_{cr}$. $\bar{S}_{cr}$ is a measure for the amount of crystals in the immediate neighborhood, influencing the crystallization kinetics at the location being evaluated. υ quantifies how important the presence of already formed crystals is on the crystallization threshold U_{thr}. A non-local formulation is developed for the function $\bar{S}_{cr}$, defining $\bar{S}_{cr}$ as:

$$\bar{S}_{cr} = \frac{\int_\Omega w_f S_{cr} \mathrm{d}\Omega}{\int_\Omega w_f \mathrm{d}\Omega} \tag{14}$$

with w_f a weighting function, defined as a multivariate normal distribution:

$$w_f = \frac{1}{(2\pi)^{\frac{k}{2}}\, l^k} \exp\left(-\frac{r^2}{2l^2}\right) \tag{15}$$

with r the distance away from the evaluated point and l the influence length. k represents the number of dimensions (1, 2 or 3). The influence length l controls the extent of the crystallization zone. The smaller the value for l is, the more localized crystallization will be; larger l-values lead to crystallization that is more spread over the domain Ω.

2.4. Conservation of momentum

The solid momentum balance, in absence of body forces, reads:

$$\nabla \cdot \boldsymbol{\sigma}_s = 0 \tag{16}$$

with $\boldsymbol{\sigma}_s$ the partial stress tensor, expressed as:

$$\boldsymbol{\sigma}_s = \boldsymbol{\sigma} - bp_s\mathbf{I} \tag{17}$$

with $\boldsymbol{\sigma}$ the effective stress tensor, b the Biot coefficient, p_s the solid pressure and $\mathbf{I}$ the second order unit tensor. p_s accounts for the mechanical effects of the constituents in the pore space on the macroscopic behavior of the porous material. The Biot coefficient is defined as:

$$b = 1 - \frac{\tilde{K}}{\tilde{K}_s} \leq 1 \tag{18}$$

with $\tilde{K}$ the bulk modulus of the porous material (solid matrix and pore space) and $\tilde{K}_s$ the bulk modulus of the solid matrix.

The solid pressure is defined according to the theory of poromechanics (Coussy, 2004, 2010):

$$p_s = \sum_j \left[S_j \left(p_j - p_{0,j}\right)\right] \tag{19}$$

where j represents the different phases present in the pore space, being gas, liquid and crystal. p_j is the pressure exerted by phase j and $p_{0,j}$ is the pressure which accounts for the averaged pressure shift induced by the interface stress, $2\sigma_{s,j}/r$, between the phase and the solid matrix, with respect to the possible values of the pore radius r (Coussy, 2010). The pressure $p_{0,j}$ is expressed as (Coussy, 2010):

$$p_{0,j} = \frac{1}{S_j}\int_0^\infty \frac{2\sigma_{s,j}}{r}\frac{\mathrm{d}S_j}{\mathrm{d}r}\mathrm{d}r \tag{20}$$

It is generally assumed that there is a thin liquid film between the salt crystal and the solid matrix (see Figure 1) (Scherer, 2004; Steiger, 2005a). Thus there is no direct interface between the salt crystal and the solid matrix. Therefore, we assume that we can omit the interfacial stress between the crystal phase

and the solid phase ($p_{0,cr}$) and we consider only the interfacial stress between solid and gas phase and solid and liquid phase, $p_{0,g}$ and $p_{0,l}$, respectively. The solid pressure is then expressed as:

$$p_s = S_g p_g + S_l p_l + S_{cr} p_{cr} - S_g p_{0,g} - (S_l + S_{cr})\, p_{0,l} \tag{21}$$

Using the relationship $S_g + S_l + S_{cr} = 1$ and the definition of capillary pressure, equation 2, and defining the crystallization pressure p_x as the difference between the pressure of the crystal phase and the pressure of the liquid phase $p_x = p_{cr} - p_l$, equation 21 becomes:

$$p_s = p_g + (S_l + S_{cr})\, p_c + S_{cr} p_x - S_g p_{0,g} - (S_l + S_{cr})\, p_{0,l} \tag{22}$$

where $p_{0,l}$ is defined as:

$$p_{0,l} = \frac{1}{S_l + S_{cr}} \int_0^\infty \frac{2\sigma_{s,l}}{r} \frac{\mathrm{d}\,(S_l + S_{cr})}{\mathrm{d}r} \mathrm{d}r \tag{23}$$

and $p_{0,g}$ as:

$$p_{0,g} = \frac{1}{S_g} \int_0^\infty \frac{2\sigma_{s,g}}{r} \frac{\mathrm{d}\,(S_g)}{\mathrm{d}r} \mathrm{d}r = -\frac{1}{S_g} \int_0^\infty \frac{2\sigma_{s,g}}{r} \frac{\mathrm{d}\,(S_l + S_{cr})}{\mathrm{d}r} \mathrm{d}r \tag{24}$$

Knowing that $\frac{2\sigma_{s,l}}{r} - \frac{2\sigma_{s,g}}{r}$ equals the capillary pressure p_c, we can write:

$$p_s = p_g + (S_l + S_{cr})\, p_c + S_{cr} p_x - \int_0^\infty p_c \frac{\mathrm{d}\,(S_l + S_{cr})}{\mathrm{d}r} \mathrm{d}r \tag{25}$$

Starting from a reference state $p_s = 0$ defined by $p_g = p_{atm}$, $p_c = p_{c,ref}$ and $p_x = p_{x,ref}$, and assuming that the gas pressure is constant and equal to the atmospheric pressure, equation 25 becomes:

$$p_s = \int_{p_{c,ref}}^{p_c} (S_l + S_{cr})\, \mathrm{d}p_c + S_{cr}\,(p_x - p_{x,ref}) \tag{26}$$

The effective stress tensor $\boldsymbol{\sigma}$ is given by:

$$\boldsymbol{\sigma} = \boldsymbol{D}\left(\boldsymbol{\epsilon} - \boldsymbol{\epsilon}_T\right) \tag{27}$$

where $\boldsymbol{D}$ is the 4^{th} order elasticity tensor, assuming that the porous material exhibits linear elastic mechanical behavior. $\boldsymbol{\epsilon}$ is the second order strain tensor equal to the symmetric gradient of the displacement field $\mathbf{u}$ under the assumption of small deformations:

$$\boldsymbol{\epsilon} = \nabla^{sym}\mathbf{u} \tag{28}$$

$\boldsymbol{\epsilon}_T$ is the thermal strain tensor, accounting for the thermal expansion or contraction of the porous material:

$$\boldsymbol{\epsilon}_T = \alpha\mathbf{I}\left(T - T_{ref}\right) \tag{29}$$

with α the thermal expansion coefficient of the porous material and T_{ref} the reference temperature.

2.5. Damage

We assume that damage occurs, i.e. that a crack develops, when the j^{th} principal component σ_j of the effective stress tensor, determined from equation 16 using definitions 17 and 27, exceeds the material strength f_t^0. This is expressed by the following criterion:

$$f = \sigma_j - f_t^0 \leqslant 0 \tag{30}$$

If equation 30 is violated at a material point, a crack surface develops normal to the j^{th} principal stress direction. The dependence of the material strength on the liquid saturation degree S_l is accounted for in the model (see equation 38).

3. Drying experiment, material and salt properties

3.1. Drying experiment

Drying of a Savonnières limestone sample (10x10x8.5 mm^3) at 45°C, initially saturated with a 5.8 molal sodium chloride solution, has been visualized and quantified using quantitative neutron imaging analysis (Derluyn, 2012). The moisture content resolution with this technique amounts to 0.04 kg/m^3. The sample was prepared by applying a water and vapor tight membrane on the lateral sides (aluminum tape) in order to create a one-dimensional drying process. Drying occurred in the direction perpendicular to the bedding of Savonnières limestone. A hydrophobic treatment (SILRES BS 280, Wacker) was applied on the upper 3 mm of the sample. Drying could only occur through the hydrophobically treated upper part as the bottom surface was sealed. The hydrophobic treatment was intended to prevent salt efflorescence and induce in-pore crystallization. During the drying, the neutron radiographs of high spatial resolution (nominal pixel size of 13.5 μm) indicated considerable deformations after about 100 minutes. These deformations are induced by crack formation due to the crystallization of sodium chloride. The cracks resulting from the salt crystallization were characterized using X-ray micro-computed tomography. The experiment revealed that the salt crystals precipitate in the upper region of the sample, mainly in the hydrophobic zone, but below the top surface of the sample. Consequently, cracks formed in this zone (see Figure 3).

3.2. Savonnières properties

The total open porosity Φ of the Savonnières limestone used for the experimental study was determined by vacuum saturation and amounts 26.9%. The density of the limestone equals 1975 kg/m^3. During capillary saturation, only 56% of the pore space gets filled, or the capillary active porosity of untreated Savonnières limestone amounts $\Phi_{unt} = 14.9\%$. The other pores are only active in the over-capillary regime (Carmeliet and Roels, 2002). When a hydrophobic treatment is applied, the treatment occupies a fraction of the pore space, defined by the porosity Φ_h. The capillary active pore space reduces to $\Phi_{unt} - \Phi_h$. The porosity affected by the hydrophobic treatment, Φ_h, at a certain position x is found by:

$$\Phi_h(x) = \Phi_{unt} - \frac{w_{l,cap}(x)}{\rho_l} \tag{31}$$

with $w_{l,cap}(x)$ the capillary moisture content at the position x, determined from the moisture profile in the capillary saturated sample in the absence of salt crystals. As soon as salt crystals start precipitating, they as well reduce the capillary active pore space. The crystals occupy a fraction of the pore space $\Phi_{cr} = \Phi S_{cr}$ and the capillary active pore space reduces to $\Phi_{unt} - \Phi_h - \Phi_{cr}$.

The moisture retention curve of untreated Savonnières limestone, describing the liquid saturation degree $S_{l,unt}$ in function of capillary pressure, is approximated by a sum of power functions (van Genuchten, 1980; Durner, 1994):

$$S_{l,unt}(p_c) = \sum_{j=1}^{s} l_j (1 + (c_j p_c)^{n_j})^{m_j} \tag{32}$$

with s the number of pore systems, l_j weight factors, and c_j, n_j and m_j model parameters. Parameter m_j can be estimated as (van Genuchten, 1980):

$$m_j = \frac{1 - n_j}{n_j} \tag{33}$$

For the wetting moisture retention curve in the capillary regime, the parameters are given in Table 1. When the capillary active porosity is reduced by a hydrophobic treatment and/or the presence of salt crystals, the liquid saturation degree S_l is reduced in a simplified way by multiplying $S_{l,unt}$ with the factor $1 - \frac{\Phi_h}{\Phi_{unt}} - \frac{\Phi_{cr}}{\Phi_{unt}}$ (Derluyn, 2012).

The liquid permeability for pure water $K_{w,unt}$ of Savonnières limestone in function of capillary pressure was determined from the moisture profiles obtained by neutron imaging during a capillary uptake test, as explained in Derluyn et al. (2013). The liquid permeability for a salt solution $K_{l,unt}$ can be calculated from the liquid permeability of pure water as:

$$K_{l,unt} = K_{w,unt} \frac{\eta_w}{\rho_w} \frac{\rho_l}{\eta_l} \tag{34}$$

where η is the viscosity. The viscosity of sodium chloride solutions with a concentration between 0 to 6 molal in a temperature range of 20 to 150°C is given in Kestin et al. (1981). The density, as function of temperature and concentration, can be calculated following Steiger (2000, 2008). The relation expressed by equation 34 was confirmed experimentally by Derluyn et al. (2013). When the capillary active pore space is reduced by a hydrophobic treatment and/or the presence of salt crystals, the liquid permeability K_l is reduced, similar to the liquid saturation degree, by multiplying $K_{l,unt}$ with the factor $1 - \frac{\Phi_h}{\Phi_{unt}} - \frac{\Phi_{cr}}{\Phi_{unt}}$ (Derluyn, 2012).

The vapor permeability δ_v was measured with the 'cup method' following EN ISO 12572:2001 (CEN, 2001). The nonlinear vapor permeability can be described in function of the vapor pressure p_v as:

$$\delta_v = \delta_{v,air} \cdot \left(a + b \exp\left(c \cdot \frac{p_v}{p_{v,sat}} \right) \right) \tag{35}$$

with a, b and c parameters. The vapor permeability in air $\delta_{v,air}$ is given by Schirmer's equation (Schirmer, 1938; Ochs et al., 2008). For flow perpendicular to the bedding direction of the limestone, the parameters a, b and c amount 0.0109, 8.86×10^{-6} and 8.55, respectively.

The thermal conductivity λ was measured using the heat flow meter method (EN 1946-3:1999, SIA (1999)). An average thermal conductivity of 0.99 W/mK was found for dry Savonnières limestone. To incorporate the influence of moisture, the thermal conductivity of water λ_w, multiplied with the volume fraction of water, is added to the dry thermal conductivity:

$$\lambda\left(S_l\right) = \lambda_{dry} + \lambda_w \Phi S_l \tag{36}$$

Values for λ_w are given by Haynes and Lide (2012), e.g. at 20°C λ_w equals 0.6 W/mK . The thermal capacity $c_{p,s}$ of Savonnières limestone is estimated to be 900 J/kgK (www.engineeringtoolbox.com). The thermal expansion coefficient α was determined by measuring the thermal dilation in a dynamic mechanical analyser (DMA 7e, Perkin Elmer) during a heating-cooling cycle (125°C - 25°C), an average value of 5.5 µm/mK was obtained.

The E-modulus was measured on samples of 16 cm height and 4 x 4 cm^2 cross section. The samples were subjected to a compressive load up to $1/3^{rd}$ of their compressive strength. During this compression the deformation was measured using a strain gauge, and the E-modulus was determined from

the load-deformation curve. In the dry state, an average E-modulus of 13.9 GPa is found perpendicular to the bedding direction. When the stone is capillary saturated, the E-modulus perpendicular to the bedding direction reduces to 11.2 GPa. The change of E-modulus with saturation degree can be approximated by:

$$E\left(S_l\right) = E_{wet} + \left(E_{dry} - E_{wet}\right) \exp\left(-p \frac{\Phi}{\Phi_{unt}} S_l\right) \tag{37}$$

with p a parameter, determined from experiments. We adopt a value of 36 (Poupeleer, 2007), but remark that this value was determined on calcium silicate board. The function in equation 37 expresses that the E-modulus decreases rapidly to the E-modulus of the wet state when the stone becomes wet ($S_l > 0$). The same behavior was, for example, observed by Van Den Abeele et al. (2002) on Meule sandstone.

The tensile strength of dry Savonnières limestone was determined from a tensile test. In the direction perpendicular to the bedding, the tensile strength $f^0_{t_{dry}}$ equals 1.8 MPa. The tensile strength of the bulk material in function of liquid saturation degree can be written as:

$$f^0_t\left(S_l\right) = \frac{f^0_{t_{dry}}}{E_{dry}} E\left(S_l\right) \tag{38}$$

assuming the same tensile strain in dry and wet conditions.

The Biot coefficient of Savonnières limestone was not measured experimentally, but estimated from literature data of a similar limestone (Lion et al., 2004). A value of 0.77 is assumed.

3.3. Sodium chloride properties

The sodium chloride diffusion coefficient in the porous material, $\mathbf{D}_i^l$, is defined by Buchwald (2000) as:

$$\mathbf{D}_i^l = \boldsymbol{\tau}^{-1} D\left(C,T\right) \Phi {S_l}^n \tag{39}$$

where $D\left(C,T\right)$ is the diffusion coefficient in function of concentration and temperature in a non-dilute solution, taken from Rard and Miller (1979), $\boldsymbol{\tau}$ is the tortuosity of the porous material, being 24.4 perpendicular to the bedding direction, and n is the saturation exponent, taken equal to 1.6 (Buchwald, 2000).

To estimate the heat of crystallization L_{cr}, the method described by Marliacy et al. (2000) is adopted, as described by Derluyn (2012). The heat capacity $c_{p,cr}$ of sodium chloride crystals is obtained from Haynes and Lide (2012).

The supersaturation U and the water activity a_w are calculated using the Pitzer ion interaction approach as described by Steiger et al. (2008), thus accounting for the non-ideal behavior of pore solutions. The supersaturation and the water activity are both function of the temperature and the salt concentration. The crystallization pressure p_x is then given by (Steiger, 2005a):

$$p_x = \frac{RT}{\bar{V}_{cr}} \ln U \tag{40}$$

with R the universal gas constant, T the absolute temperature and $\bar{V}_{cr}$ the molar volume of the crystal, being 27 cm^3/mole for sodium chloride.

The kinetic growth parameters $K_{m,cr}$ and g_{cr} for sodium chloride equal 0.41 $\mathrm{kg/m}^3\mathrm{s}$ (Espinosa-Marzal, 2009) and 1, respectively.

4. Simulation results and discussion

In this section, we simulate the coupled heat-moisture-salt transport and salt crystallization and predict the risk for salt damage for the experiment described in section 3.1. Hence, we solve equations 1, 4, 5, 8 and 16 and check when the damage criterion (equation 30) is violated. The equations are solved using the finite element method to obtain the variation of the primary variables p_c, C, T, S_{cr} and $\mathbf{u}$ in space and time. In order to obtain a mass and energy conservative system of equations, a mixed form of the capacitive terms is used, as described in Janssen et al. (2007). A staggered solution scheme is used and each equation is solved implicitly using the Newton-Raphson method. Numerical integration is performed by means of a Gauss-Lobatto scheme. This has a similar accuracy as the more commonly used Gauss-Legendre scheme, but suppresses oscillations in the solution field for our set of highly non-linear PDE's.

4.1. Input, initial and boundary conditions

The physical properties of Savonnières limestone and sodium chloride as given in sections 3.2 and 3.3 are used. The parameters υ, l and U_{start} in the U_{thr}-function (equation 13), which are related to the crystallization kinetics, are the only parameters that cannot be determined from literature or experiments. Therefore, the sensitivity of the results with respect to these three parameters is assessed by conducting a parameter study. We perform the simulation using an U_{start}-value of 1.5 or 2, a l-value of 1×10^{-4} or 1×10^{-3} m and a υ-value of $10\frac{\Phi}{\Phi_{unt}}$, $100\frac{\Phi}{\Phi_{unt}}$ or $1000\frac{\Phi}{\Phi_{unt}}$, resulting in 12 different cases. The U_{start}-value of 1.5 corresponds to a concentration increase of 9% by mass

with respect to the saturated concentration at 45°C (based on Steiger et al. (2008)). This value is close to the maximal value of 10% mentioned by Flatt (2002).

The simulation is performed on a 1-dimensional mesh of length L, where L equals the height of the sample used in the drying experiment, being 8.19 mm. We acknowledge that the simulation does not completely represent the 3-dimensional nature of the sample. However, the drying process itself, inducing the crystallization damage, can be considered to be mainly 1-dimensional. As such, the crystallization and mechanical analysis can, in a first approximation, be regarded as 1-dimensional. The mesh consists of 100 equidistant elements. The same time step is used for all discretized equations. The time step is in the order of 1 to 5 ms, assuring convergence of the coupled system of equations.

The initial capillary pressure at time $t = 0$ equals -100 Pa for every position in the sample, corresponding to the capillary saturated state. The initial temperature of the sample is equal to 45°C. The initial concentration at every position in the sample equals 5.8 molal. In the initial state, no crystals are present in the sample.

The environment surrounding the sample during the experiment is characterized by a relative humidity RH_{env} of 5% and a temperature T_{env} of 45°C. Boundary conditions of the Neumann type are imposed on the top surface of the sample, being:

$$\bar{q}_m = CMTC(p_{v,env} - p_{v,surf}) \text{ with } p_{v,env} = p_{v,sat}\left(T_{env}\right) \cdot RH_{env} \tag{41}$$

$$\bar{q}_e = HTC\left(T_{env} - T_{surf}\right) + \left(c_{p,v}\left(T_{surf} - T_0\right) + L_v\right) \cdot \bar{q}_m \tag{42}$$

with $\bar{q}_m$ the moisture flux and $\bar{q}_e$ the heat flux at the boundary. $p_{v,surf}$ and

T_{surf} are the vapor pressure and the temperature at the boundary surface. The convective mass transfer coefficient $CMTC$ is determined based on inverse modeling (Derluyn, 2012) and amounts 3.95×10^{-9} s/m. The convective heat transfer coefficient $CHTC$ is then given by the Chilton-Colburn analogy (Chilton and Colburn, 1934) and amounts 0.57 W/m^{2}K. The radiative heat transfer coefficient $RHTC$ is 5.1 W/m^{2}K (CEN, 2004) and the corresponding total heat transfer coefficient HTC is thus 5.67 W/m^{2}K. Zero-flux boundary conditions are applied on the bottom side of the sample.

4.2. Results and discussion

From the experimental results, we know that the sample starts to deform considerably after 100 minutes, due to crack formation. We expect that the effective stress at a certain position in the sample exceeds the tensile strength around this time. With this assumption, we consider the material to mechanically behave homogeneously; and we remark that this approximation does not explicitly account for the existence of local weak spots in the microstructure of the stone. An overview of the maximal effective stress reached after 2.5 hours of drying is given in Table 2 using different values for the parameters U_{start}, l and υ. Only four of the twelve sets of parameters predict damage within the simulated time frame. The table indicates that the more crystals can spread within the sample (larger l value) and the faster the U_{thr}-function reduces to 1 (larger υ value), the longer it takes before the effective stress exceeds the tensile strength.

We will further discuss three simulation results more in detail. We select the U_{start}-value of 1.5, which is the closest to the maximal value expected by Flatt (2002). We compare the simulation result using $l = 1 \times 10^{-4}$ and

$\upsilon = 100$, that results in damage after 114 minutes, with the simulation results using $l = 1 \times 10^{-4}$ and $\upsilon = 1000$ and using $l = 1 \times 10^{-3}$ and $\upsilon = 100$, which do not yield damage within the considered time period. The comparison is done for the first 114 minutes of the simulation. The parameter set with $l = 1 \times 10^{-4}$ and $\upsilon = 100$ gives the best agreement with the experimental result, whereas the other two parameter sets show the influence of different crystallization kinetics. The U_{start}-value of 1.5 is reached after 23 minutes. The effective stress and the strain evolution with time are given by the profiles in Figure 2. We observe that the highest stresses (Figure 2a) and strains (Figure 2d) develop at about 0.4 mm from the top of the sample. This is in agreement with the observed crack pattern in the sample. A vertical slice obtained from the X-ray tomographic dataset of the sample after the drying experiment is shown in Figure 3. A crack developed at the same position as where the effective stress reaches the tensile strength of 1.58 MPa.

The effective stresses in Figures 2a, 2b and 2c are directly related to the crystal saturation degree S_{cr} and the crystallization pressure p_x. It is the product of these two quantities that determines the effective stress, as expressed by equation 26. The profiles of S_{cr} and p_x are given in Figure 4. In the simulation with $l = 1 \times 10^{-4}$ and $\upsilon = 100$, the highest amount of crystals is reached locally (Figure 4a), and the crystallization zone in the sample is small. When changing the υ-value to 1000, the maximal S_{cr}-value reduces and the crystals are a little more spread (Figure 4b). When changing the l-value to 1×10^{-3} there is significantly more spreading of crystals, and the maximal S_{cr}-value consequently reduces further (Figure 4c). The crystallization pressure is related to the concentration evolution,

given in Figures 5a, 5b and 5c. The concentration, and consequently the crystallization pressure, increase due to the drying process, and decrease due to the salt crystallization. The concentration in Figure 5b decreases faster in the crystallization zone than in Figure 5a due to the larger value for the parameter υ, and thus a faster decrease of the U_{thr}-value. The concentration in Figure 5c also decreases faster due to the larger parameter l, representing a larger influence length, and thus a larger crystallization zone. The moisture content profiles of the different simulations (Figures 5d, 5e and 5f) do not show a large difference. The difference is mainly in the upper part of the sample, where the crystals precipitate as indicated by the gray arrow in the figures.

As our sample can deform freely, the solid stress $\boldsymbol{\sigma}_s$ equals zero (i.e. is equal to the external mechanical stress). This means that the effective stress $\boldsymbol{\sigma}$ is only determined by the solid pressure p_s. Using equation 26 and considering that our simulation is 1-dimensional, so that we can denote the stresses by a scalar (i.e. we describe the stress along the height of the sample), gives:

$$\begin{aligned} \sigma &= b\left(\int_{-100}^{p_c}\left(S_l + S_{cr}\right)\mathrm{d}p_c + S_{cr}p_x\right) \\ &= b\left(\int_{-100}^{p_c}\left(S_{l,unt}\left(1-\frac{\Phi_h}{\Phi_{unt}}\right)\right)\mathrm{d}p_c + S_{cr}p_x\right) \end{aligned} \tag{43}$$

The effect of the hygric stresses, expressed by the first term in equation 43 is found to be negligible in this simulation, as they only range in the order of magnitude of 1000 Pa. Thus the effective stress, given in Figures 2a, 2b, 2c is approximately given by:

$$\sigma \approx bS_{cr}p_x \tag{44}$$

The strains in Figures 2d, 2e and 2f are related to the crystal formation and to the temperature change in the sample. The sample cools down due to evaporative cooling as represented for the boundary location, $x = L$, in Figure 6. At other positions in the sample, the temperature evolution is similar. The cooling causes a shrinkage of the sample. As the sample can deform freely and the cooling is uniform over the sample, the strains due to the cooling are uniform and no internal stresses develop due to the thermal shrinkage. When crystals start to form, they cause expansion of the sample in the zone where the crystals precipitate.

The liquid weight decrease is given in Figure 7a. The three simulations approach the experimentally obtained data. The accumulated crystal mass is given in Figure 7b. An important observation is that the case where damage is induced after 114 minutes (simulation 1 with $l = 1 \times 10^{-4}$ and $\upsilon = 100$) corresponds to the case where the lowest amount of accumulated crystal mass is found. This indicates that the risk for salt damage depends strongly on the crystallization kinetics, rather than on the amount of crystals formed. The parameter study indicates that when it is more difficult for the crystals to form (the lower l and the lower υ), the damage will occur faster once crystals start to grow. This is because higher crystallization pressures can build up and the crystals precipitate more localized, causing higher effective stresses locally. This result shows the importance of the nucleation and growth kinetics for the correct prediction of salt damage risks. It indicates that if you can control the kinetics of crystallization, you can control salt damage.

5. Conclusions

We have developed a fully coupled computational model that describes heat, water and ion transport, salt crystallization and deformations and damage induced by hygro-thermal and crystallization stresses. The model predicts the macroscopic behavior and physical degradation of porous materials. The model has been discussed with the focus on the prediction of salt damage caused by the formation of sodium chloride crystals in a porous limestone during drying. The simulation results show a good agreement with experimental data, obtained from neutron and X-ray imaging techniques, when choosing suitable parameters for the crystallization kinetics. These parameters are estimated based on a sensitivity study. The simulations show that the effective stresses resulting from salt crystallization do not only depend on the crystallization pressure, which is related to the supersaturation, but also on the amount of salt crystals forming and the localization of these crystals. In order to include the last aspect, a non-local formulation was incorporated in the model. Future research could focus on experimental and/or modeling studies for the reliable prediction of the kinetic parameters. The results presented in this paper suggest that controlling the nucleation and growth kinetics is the key factor to control crystallization damage in porous building materials.

6. Acknowledgments

The Department of Architecture at ETH Zurich is acknowledged for co-funding the research of Hannelore Derluyn.

7. Vitae

7.1. Dr. ir. Hannelore Derluyn

Hannelore Derluyn received her master degree in civil engineering from K.U. Leuven (Belgium) in July 2006, magna cum laude. Subsequently, she was a research affiliate at K.U. Leuven. She started her PhD studies there in January 2008 and pursued her research at ETH Zurich (Switzerland). She obtained her PhD degree from ETH Zurich in November 2012 and was awarded the ETH Medal. During her PhD studies, she was an academic guest at EMPA Dübendorf (Switzerland), Princeton University (USA) and Ghent University (Belgium). She was a postdoc at ETH Zurich/EMPA Dübendorf. From October 2013, she is an FWO-postdoc fellow at Ghent University.

7.2. Dr. ir. Peter Moonen

Peter Moonen studied civil engineering at K.U. Leuven (Belgium), and graduated in July 2003 with summa cum laude. After graduation, he started working on an interdisciplinary project, which resulted in a dual PhD degree, issued by both the K.U. Leuven and the Delft University of Technology (The Netherlands). In 2009-2010, he had the opportunity to do a postdoc at the ETH Zurich (Switzerland). Since the beginning of 2011, he is research scientist at Empa Dübendorf (Switzerland) and lecturer at ETH Zurich.

7.3. Prof. dr. ir. Jan Carmeliet

Since June 2008, Jan Carmeliet is full professor at the Chair of Building Physics at ETH Zurich and head of the Laboratory of Building Science and Technology of EMPA Dübendorf (Switzerland). Jan Carmeliet received his

PhD in Civil Engineering at K.U. Leuven (Belgium) in 1992 and was a post-doctoral fellow at the Delft University of Technology (The Netherlands). He has been Assistant (1998), Associate (2001) and Full Professor (2004) at K.U. Leuven and part-time Professor at the Eindhoven University of Technology (since 2001). In 2007 he was on sabbatical leave at the University of Illinois at Urbana Champaign and at Los Alamos Governmental Laboratories.

References

Buchwald, A., 2000. Determination of the ion diffusion coefficient in moisture and salt loaded masonry materials by impedance spectroscopy, in: 3rd International PhD Symposium, Vol. 2., 10-13 October 2000, Vienna, Austria, pp. 475–482.

Carmeliet, J., Roels, S., 2002. Determination of the Moisture Capacity of Porous Building Materials. J. Build. Phys. 25 (3), 209–237.

CEN, 2001. EN ISO 12572:2001 Hygrothermal performance of building materials and products - Determination of water vapour transmission properties.

CEN, 2004. prEN 15026 Hygrothermal performance of building components and building elements - Assessment of moisture transfer by numerical simulation.

Chilton, T., Colburn, A. P., 1934. Mass transfer (absorption) coefficients. Prediction from data on heat transfer and fluid friction. Ind. Eng. Chem. 26 (11), 1183–1187.

524 Coussy, O., 2004. Poromechanics, John Wiley & Sons Ltd., Chichester, UK.

525 Coussy, O., 2006. Deformation and stress from in-pore drying-induced crys-
526 tallization of salt. J. Mech. Phys. Solids 54 (8), 1517–1547.

527 Coussy, O., 2010. Mechanics and Physics of Porous Solids, first ed. John
528 Wiley & Sons Ltd., Chichester, UK.

529 Derluyn, H., 2012. Salt transport and crystallization in porous limestone:
530 neutron - X-ray imaging and poromechanical modeling, Diss. ETH No.
531 20673. Ph.D. thesis, ETH Zurich, Switzerland.

532 Derluyn, H., Griffa, M., Mannes, D., Jerjen, I., Dewanckele, J., Vontobel, P.,
533 Sheppard, A., Derome, D., Cnudde, V., Lehmann, E., Carmeliet, J., 2013.
534 Characterizing saline uptake and salt crystal distributions in porous lime-
535 stone with neutron radiography and X-ray micro-tomography. J. Build.
536 Phys. 36 (4), 353–374.

537 Durner, W., 1994. Hydraulic conductivity estimation for soils with heteroge-
538 neous pore structure. Water Resour. Res. 30 (2), 211–223.

539 Espinosa, R. M., Franke, L., Deckelmann, G., Gunstmann, C., 2007. Gekop-
540 pelter Wärme- und Stofftransport einschließlich der Korrosionsprozesse
541 in porösen Baustoffen mit dem Simulationsprogramm AStra. Bauphysik
542 29 (3), 187–193.

543 Espinosa, R. M., Franke, L., Deckelmann, G., 2008. Phase changes of salts
544 in porous materials: Crystallization, hydration and deliquescence. Constr.
545 Build. Mater. 22 (8), 1758–1773.

546 Espinosa-Marzal, R. M., 2009. Personal communication.

547 Flatt, R. J., 2002. Salt damage in porous materials: how high supersatura-
548 tions are generated. J. Cryst. Growth 242 (3-4), 435–454.

549 Haynes, W., Lide, D. (Eds.), 2012. CRC Handbook of Chemistry and Physics,
550 92nd ed. Internet Version 2012.

551 Janssen, H., 2002. The influence of soil moisture transfer on building heat
552 loss via the ground. Ph.D. thesis, K.U. Leuven, Belgium.

553 Janssen, H., Blocken, B., Carmeliet, J., 2007. Conservative modelling of
554 the moisture and heat transfer in building components under atmospheric
555 excitation. Int. J. Heat Mass Tran. 50 (5-6), 1128–1140.

556 Kestin, J., Ezzat Khalifa, H., Correia, R. J., 1981. Tables of the dynamic and
557 kinematic viscosity of aqueous NaCl solutions in the temperature range 20-
558 150°C and the pressure range 0.1-35 MPa. J. Phys. Chem. Ref. Data 10 (1),
559 71–87.

560 Koniorczyk, M., 2010. Modelling the phase change of salt dissolved in pore
561 water - Equilibrium and non-equilibrium approach. Constr. Build. Mater.
562 24 (7), 1119–1128.

563 Koniorczyk, M., 2012. Salt transport and crystallization in non-isothermal,
564 partially saturated porous materials considering ions interaction model.
565 Int. J. Heat Mass Tran. 55 (4), 665–679.

566 Lion, M., Skoczylas, F., Ledésert, B., 2004. Determination of the main hy-

draulic and poro-elastic properties of a limestone from Bourgogne, France. Int. J. Rock Mech. Min. 41 (6), 915–925.

Marliacy, P., Solimando, R., Bouroukba, M., Schuffenecker, L., 2000. Thermodynamics of crystallization of sodium sulfate decahydrate in H2O-NaCl-Na2SO4: application to Na2SO4.10H2O-based latent heat storage materials. Thermochim. Acta 344, 85–94.

Moonen, P., Sluys, L. J., Carmeliet, J., 2010. A continuous-discontinuous approach to simulate physical degradation processes in porous media. Int. J. Numer. Meth. Eng. 84, 1009–1037.

Moonen, P., Sluys, L. J., Carmeliet, J., 2011. A continuous-discontinuous approach to simulate heat transfer in fractured media. Transport Porous Med. 89 (3), 399–419.

Nicolai, A., Grunewald, J., Zhang, J. S., 2007. Salztransport und Phasenumwandlung - Modellierung und numerische Lösung im Simulationsprogramm Delphin 5. Bauphysik 29 (3), 231–239.

Ochs, F., Heidemann, W., Mullersteinhagen, H., 2008. Effective thermal conductivity of moistened insulation materials as a function of temperature. Int. J. Heat Mass Tran. 51 (3-4), 539–552.

Poupeleer, A., 2007. Transport and crystallization of dissolved salts in cracked porous building materials. Ph.D. thesis, K.U. Leuven, Belgium.

Rard, J. A., Miller, D. G., 1979. The mutual diffusion coefficients of NaCl-H2O and CaCl2-H2O at 25°C from Rayleigh interferometry. J. Solution Chem. 8 (10), 701–716.

590 Scherer, G. W., 1999. Crystallization in pores. Cement Concrete Comp. 29,
591 1347–1358.

592 Scherer, G. W., 2004. Stress from crystallization of salt. Cement Concrete
593 Res. 34, 1613–1624.

594 Schirmer, R., 1938. Die Diffusionszahl von Wasserdampf-Luftgemischen und
595 die Verdampfungs-geschwindigkeit. ZVDI Beheift Verfahrenstechnik 6,
596 170.

597 SIA, 1999. EN 1946-3:1999 Wärmetechnisches Verhalten von Bauprodukten
598 und Bauteilen - Technische Kriterien zur Begutachtung von Laboratorien
599 bei der Durchführung der Messungen von Wärmeübertragungseigenschaften
600 - Teil 3: Messung nach dem Verfahren mit dem Wärmestrom.

602 Steiger, M., 2000. Chapter 6: Total volumes of crystalline solids and salt
603 solutions, in: Price, C. (Ed.), An expert chemical model for determining
604 the environmental conditions needed to prevent salt damage in porous
605 materials, pp. 53–63.

606 Steiger, M., 2005a. Crystal growth in porous materials - I: The crystallization
607 pressure of large crystals. J. Cryst. Growth 282 (3-4), 455–469.

608 Steiger, M., 2005b. Crystal growth in porous materials - II: Influence of
609 crystal size on the crystallization pressure. J. Cryst. Growth 282 (3-4),
610 470–481.

611 Steiger, M., 2008. Personal communication.

612 Steiger, M., Kiekbusch, J., Nicolai, A., 2008. An improved model incorpo-
613 rating Pitzer's equations for calculation of thermodynamic properties of
614 pore solutions implemented into an efficient program code. Constr. Build.
615 Mater. 22 (8), 1841–1850.

616 Van Den Abeele, K. E.-A., Carmeliet, J., Johnson, P. A., Zinszner, B., 2002.
617 Influence of water saturation on the nonlinear elastic mesoscopic response
618 in Earth materials and the implications to the mechanism of nonlinearity.
619 J. Geophys. Res. 107, 2121.

620 van Genuchten, M. T., 1980. A closed-form equation for predicting the hy-
621 draulic conductivity of unsaturated soils. Soil Sci. Soc. Am. J. 44, 892–898.

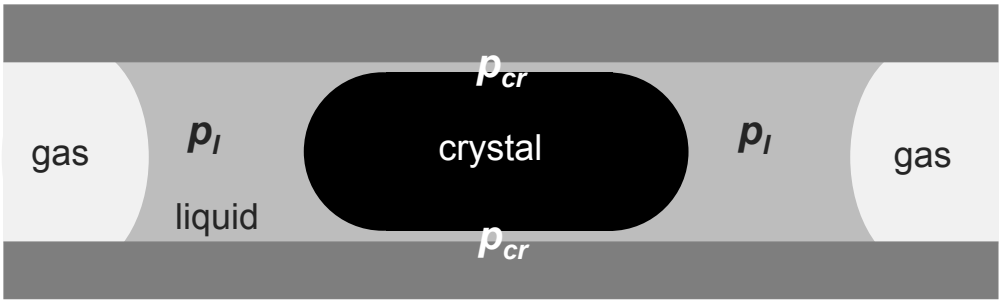

Figure 1: Schematic illustration of a crystal in a pore. A liquid film is maintained between the crystal surface and the pore wall.

Table 1: Parameters for the analytical fit of the capillary water retention curve.

i	1	2	3
c_i	8.0×10^{-7}	7.0×10^{-6}	1.3×10^{-4}
n_i	4.27	1.98	1.85
l_i	0.135	0.256	0.165

Table 2: Maximal principal effective stress $\sigma_{I,max}$ after 2.5 hours using different parameter values, the height at which this effective stress is reached in the sample, and the time at which cracking occurs if the principal effective stress exceeds the tensile strength. The '-' symbol indicates that no cracks formed during the first 2.5 hours. The simulations indicated in bold are discussed further in detail.

U_{start}	l	υ	$\sigma_{I,max}$	height	time to crack
	m		MPa	mm	min.
1.5	1×10^{-3}	10	1.03	7.78	-
1.5	$\mathbf{1\times10^{-3}}$	**100**	**0.42**	**7.86**	-
1.5	1×10^{-3}	1000	0.41	7.86	-
1.5	1×10^{-4}	10	$> f_t^0$	7.86	89
1.5	$\mathbf{1\times10^{-4}}$	**100**	$\boldsymbol{> f_t^0}$	**7.78**	**114**
1.5	$\mathbf{1\times10^{-4}}$	**1000**	**1.06**	**7.62**	-
2.0	1×10^{-3}	10	1.48	7.86	-
2.0	1×10^{-3}	100	0.31	7.86	-
2.0	1×10^{-3}	1000	0.28	7.86	-
2.0	1×10^{-4}	10	$> f_t^0$	7.86	113
2.0	1×10^{-4}	100	$> f_t^0$	7.86	115
2.0	1×10^{-4}	1000	0.95	7.62	-

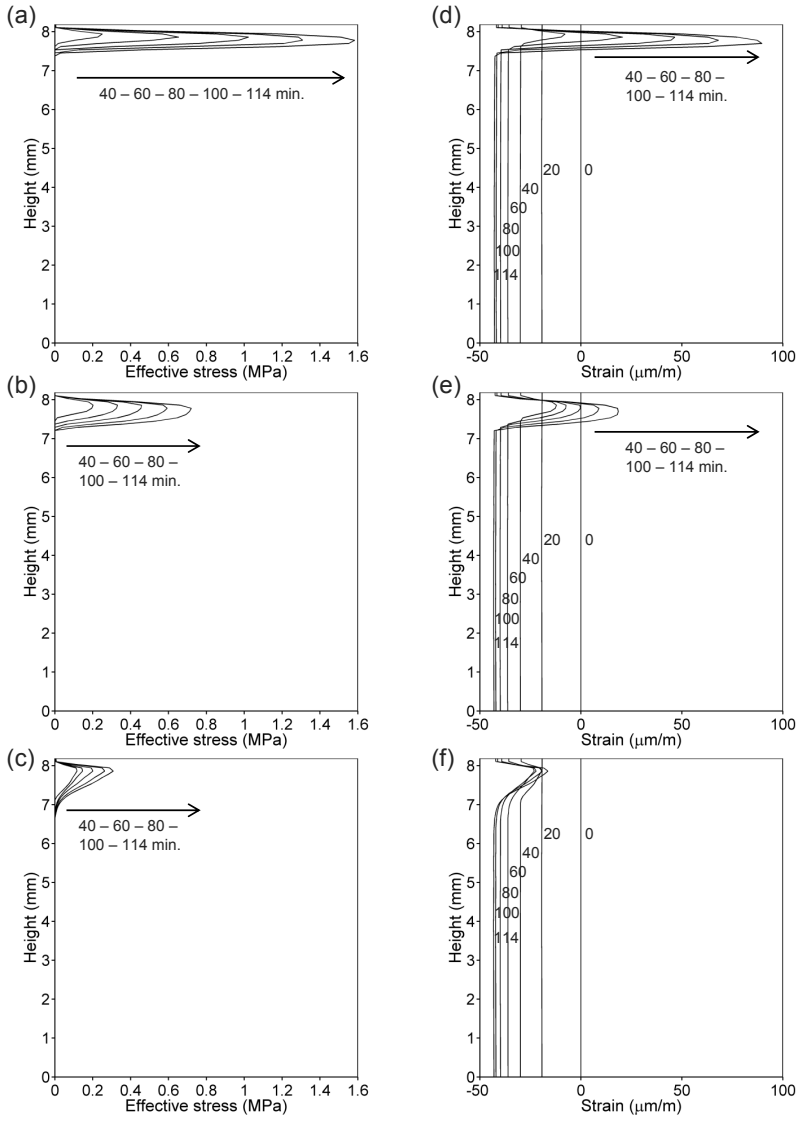

Figure 2: Effective stress (a-b-c) and strain (d-e-f) over the height of the sample for different model parameters: (a)&(d) $l = 10^{-4}$, $\upsilon = 100$, (b)&(e) $l = 10^{-4}$, $\upsilon = 1000$, (c)&(f) $l = 10^{-3}$, $\upsilon = 100$. Crystallization starts after 23 minutes.

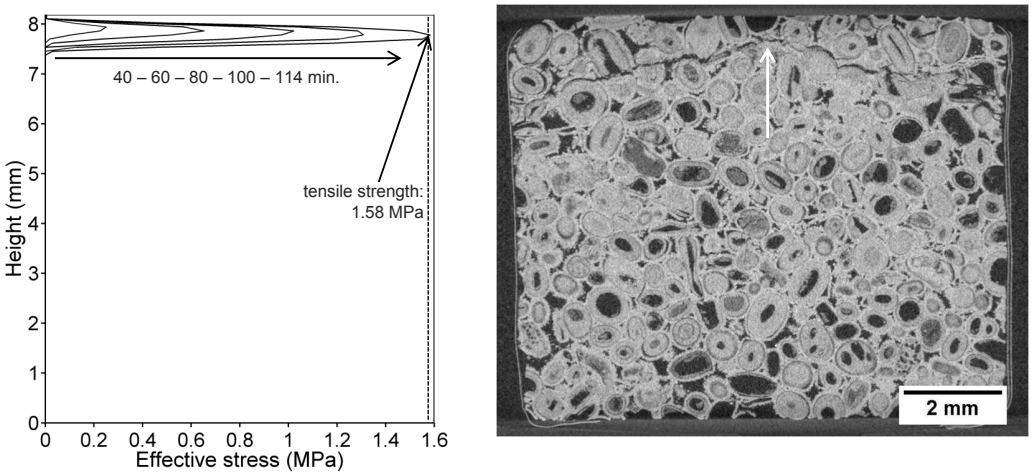

Figure 3: Comparison between the effective stress evolution, simulated with $l = 10^{-4}$, $\upsilon = 100$ (Figure 2a) and the crack pattern in the sample visualized with X-ray micro-tomography. A crack is observed at the position where the maximal effective stress develops in the simulation.

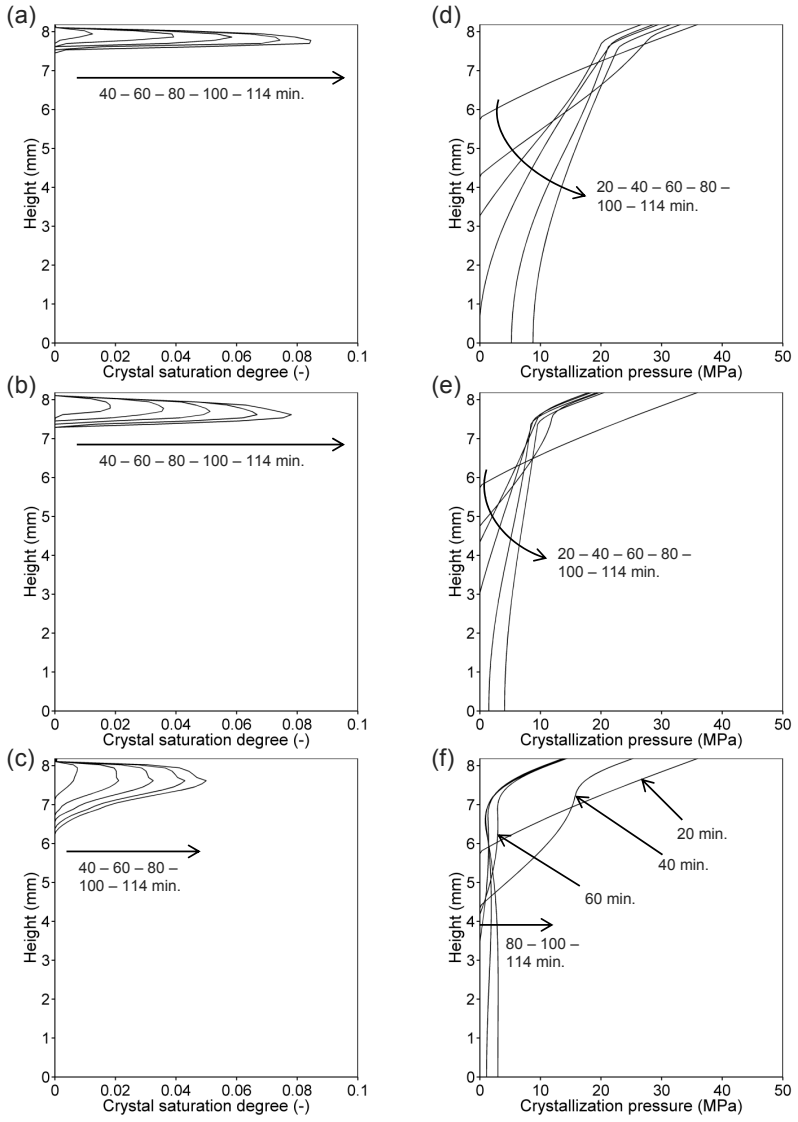

Figure 4: Salt crystallization degree (a-b-c) and crystallization pressure (d-e-f) over the height of the sample with different model parameters: (a)&(d) $l = 10^{-4}$, $\upsilon = 100$, (b)&(e) $l = 10^{-4}$, $\upsilon = 1000$, (c)&(f) $l = 10^{-3}$, $\upsilon = 100$. Crystallization starts after 23 minutes.

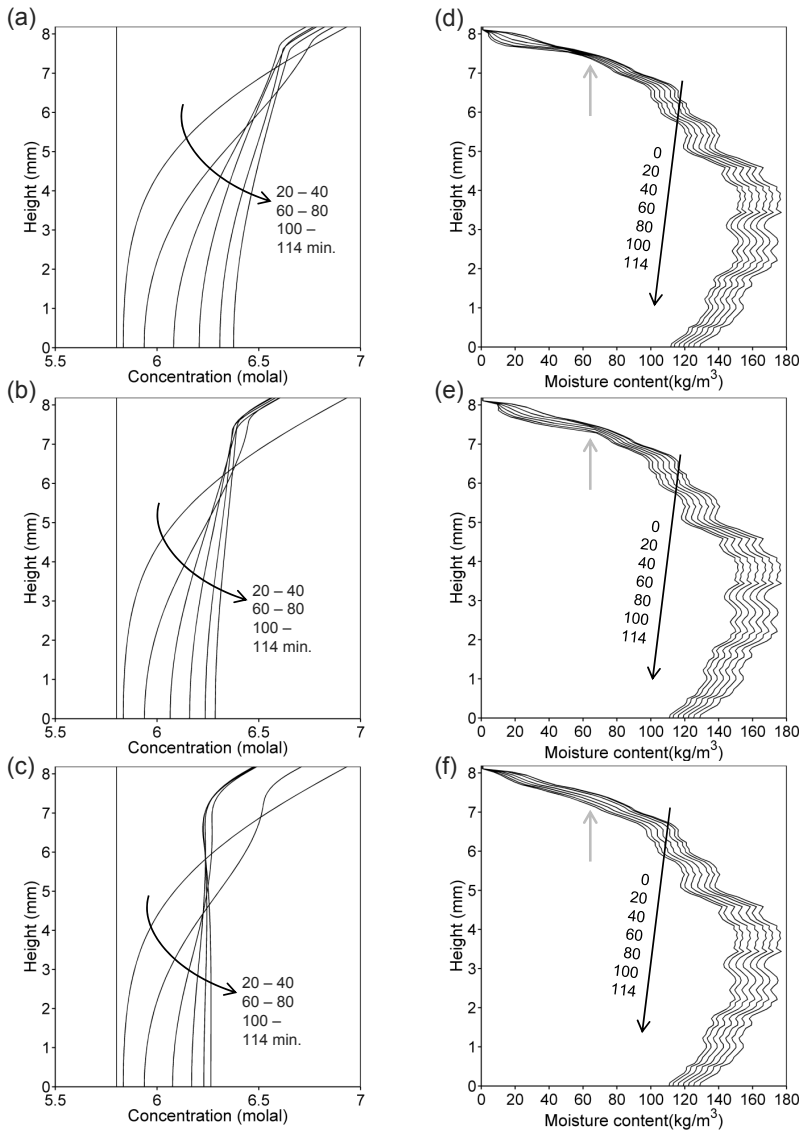

Figure 5: Salt concentration (a-b-c) and moisture content (d-e-f) over the height of the sample with different model parameters: (a)&(d) $l = 10^{-4}$, $\upsilon = 100$, (b)&(e) $l = 10^{-4}$, $\upsilon = 1000$, (c)&(f) $l = 10^{-3}$, $\upsilon = 100$. Crystallization starts after 23 minutes. The gray arrows in figures d-e-f indicate where the main difference in the moisture profiles can be observed.

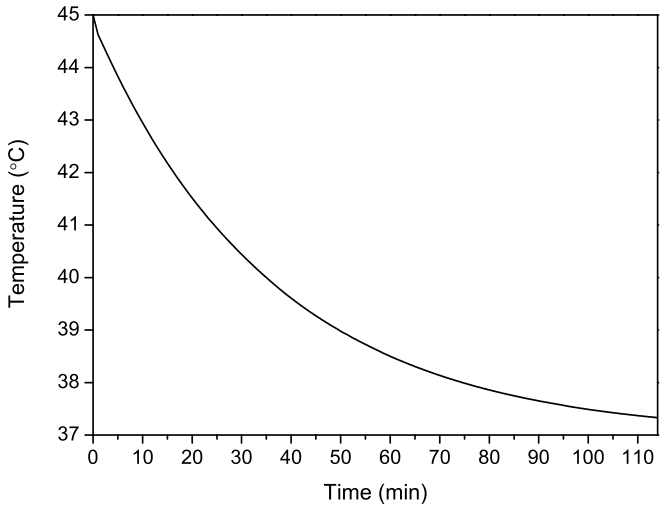

Figure 6: Temperature evolution at the boundary $x = L$ during drying. At other locations in the sample, the temperature evolution is similar.

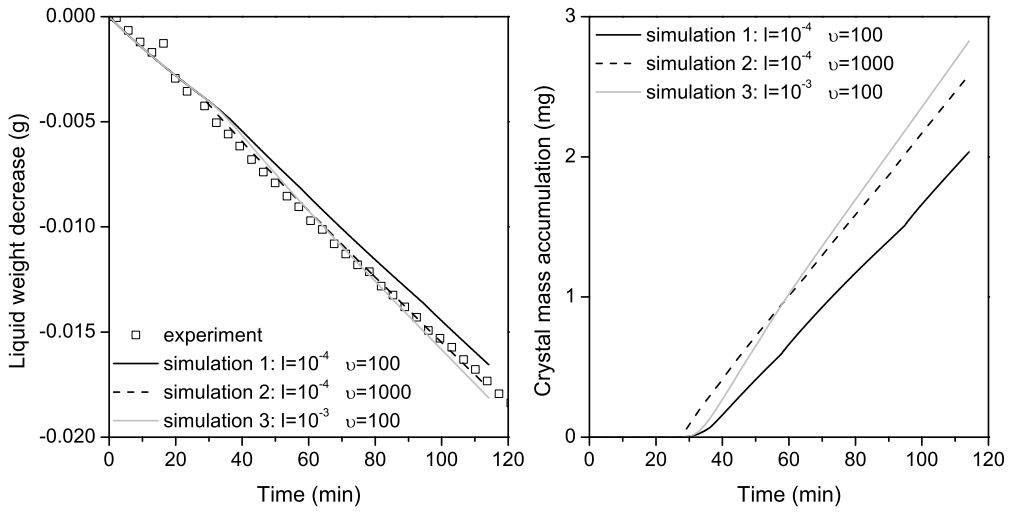

(a) (b)

Figure 7: (a) Weight decrease and (b) salt accumulation in the sample using different model parameters for nucleation: (1) $l = 10^{-4}$, $\upsilon = 100$, (2) $l = 10^{-4}$, $\upsilon = 1000$, (3) $l = 10^{-3}$, $\upsilon = 100$.